Materials Advances

ROYAL SOCIETY OF CHEMISTRY

REVIEW

View Article Online
View Journal | View Issue

Check for updates

Cite this: *Mater. Adv.*, 2024, 5, 5351

Thermoelectric materials for space explorations

Dulyawich Palaporn,[a] Sora-at Tanusilp,*[b] Yifan Sun,[c] Supree Pinitsoontorn[ad] and Ken Kurosaki*[c]

Received 23rd March 2024,
Accepted 24th May 2024

DOI: 10.1039/d4ma00309h

rsc.li/materials-advances

This comprehensive review examines the historical development of radioisotope thermoelectric generators (RTGs) over the last fifty years and anticipates future missions, providing insights into the meticulous selection of radioisotope heat sources and thermoelectric (TE) materials throughout the generations of RTGs. It analyzes the TE properties of conventional materials and investigates strategies to improve them, with a special emphasis on a dual-principle approach to increase the dimensionless figure of merit (zT). As advancements in TE materials and RTG design continue, the focus extends beyond TE properties to include other critical factors for effective RTG integration such as durability, safety, and weight.

1. Introduction

The thermoelectric (TE) effect, characterized by the Seebeck and Peltier effects, facilitates the efficient conversion of heat into electrical energy and *vice versa*. This principle underlies the operation of diverse TE devices, commonly referred to as thermoelectric generators (TEGs), which serve as promising alternatives for energy generation. A standard TEG module consists of TE couples made of p- and n-type materials, interconnected by metallic electrodes arranged in series in a π-shaped configuration, as illustrated in Fig. 1. Ceramic plates are used to establish thermal contact between the electrodes and the hot (heat source) and cold (heat sink) sides. This design ensures longitudinal heat transfer within the TE material, while the electrical current flows perpendicularly to the direction of heat flow. Additionally, the integration of diffusion barriers prevents any inter-material reactions, stabilizing contact resistance and extending the lifespan of TEGs.

The traditional module design, as shown in Fig. 1 (left), is widely used due to its straightforward design and ease of assembly, contributing to its low production costs. Nevertheless, the demanding requirements of space mission

---

[a] Department of Physics, Faculty of Science, Khon Kaen University, Khon Kaen 40002, Thailand
[b] Faculty of Engineering, Khon Kaen University, Khon Kaen 40002, Thailand. E-mail: sorata@kku.ac.th
[c] Institute for Integrated Radiation and Nuclear Science, Kyoto University, 2, Asashiro-Nishi, Kumatori, Sennan-gun, Osaka 590-0494, Japan. E-mail: kurosaki.ken.6n@kyoto-u.ac.jp
[d] Institution of Nanomaterials Research and Innovation for Energy, Faculty of Science, Khon Kaen University, Khon Kaen 40002, Thailand

Dulyawich Palaporn

Dulyawich Palaporn received his PhD in Physics from Department of Physics, Khon Kaen University, Thailand, in 2023. Currently, he is working as a Postdoctoral at Department of Physics, Khon Kaen University. His research interests include thermoelectric materials and flexible thermoelectric devices-based polymer and cellulose nanocomposites.

Sora-at Tanusilp

Sora-at Tanusilp earned his PhD in Sustainable Energy and Environmental Engineering from the Graduate School of Engineering at Osaka University, Japan, in 2019. Currently, he holds the position of lecturer in Electrical Engineering at Khon Kaen University, Thailand. His research interests primarily revolve around the study of thermoelectric materials, as well as the exploration of electronic properties within metallic and polymer matrix composites.

necessitates high efficiency and a long service life, leading to the development of a segmented design, as shown in Fig. 1 (right). This innovative design can outperform the traditional modules through the proper selection and matching of TE materials. Additionally, it also allows for the alignment of thermal expansion coefficients between p- and n-type materials to reduce torque damage. However, the segmented design is more complicated to assemble compared to traditional modules, which increases production costs and requires comprehensive stability testing, potentially over many years, before operation.

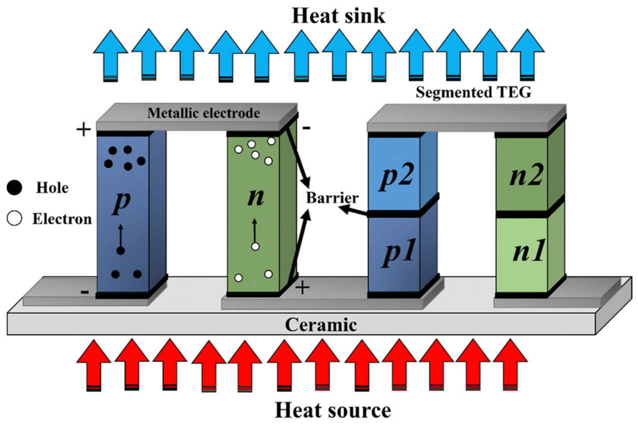

Fig. 1 Thermoelectric (TE) couples, composed of p-type and n-type materials, are connected by metallic electrodes arranged in a series with a π-shaped configuration. A traditional module (left-handed figure) has only one material in a singular leg, while the segmented TE (right-handed figure) module is characterized by the integration of two different materials.

Some of the main applications of TEGs lie in serving as primary electric power sources in specialized scenarios, including deep space exploration, planetary surface missions, orbital endeavors, and other isolated environments.[1] Due to their ability to generate electricity without any moving parts, TEGs not only provide a noiseless and vibration-free operating environment but also avoid damaging nearby systems throughout its extended service life.[2]

In 1954, the first application of TEGs to convert heat from the polonium-210 (^{210}Po) into electricity using chrome-constantan thermocouples marked the inception of the radioisotope thermoelectric generator (RTG).[3,4] In the 1960s, the National Aeronautics and Space Administration (NASA) introduced TEGs as a power source for its space program. Subsequently, RTGs have been deployed in various NASA space missions, including Galileo (1989, Jupiter), Ulysses (1990, solar mission), Cassini (1997, Saturn), New Horizons (2006, deep space mission), and Curiosity (2012, Mars).[5,6] These missions utilized RTGs with Plutonium-238 (^{238}Pu) as the heat source, employing tellurium (Te) alloys within moderate temperature ranges (500–800 K) and silicon–germanium (SiGe) alloys at higher temperatures ($>$800 K). In contrast, the European space

---

Yifan Sun

Yifan Sun is an Assistant Professor at the Institute for Integrated Radiation and Nuclear Science at Kyoto University. He holds a BS in Materials Science and Engineering from Northwestern University (2016) and an MS/PhD in Sustainable Energy and Environmental Engineering from Osaka University (2022). His research focuses on exploring machine learning for material discovery in thermoelectric and nuclear materials. Yifan is a member of the Atomic Energy Society of Japan and the Japan Society of Thermophysical Properties.

Supree Pinitsoontorn

Supree Pinitsoontorn received his DPhil in Materials from Department of Materials, University of Oxford, UK, in 2008. He is currently working as a Professor in Physics at Khon Kaen University, Thailand. His research interests include thermoelectric materials, magnetic nanoparticles, geopolymers, and bacterial cellulose nanocomposites. He has authored over 170 articles and has an H-index of 28 (Scopus).

Ken Kurosaki

Ken Kurosaki, born in 1973 in Tokushima Prefecture, Japan, serves as a Professor at Kyoto University (Institute for Integrated Radiation and Nuclear Science). He obtained his BE (1995), ME (1997), and PhD (2003) in Nuclear Engineering from Osaka University. Prior to his current position, he held roles as an Assistant Professor (1998–2009) and an Associate Professor (2009–2019) at Osaka University. His current interests focus on nuclear human resource development and innovation in the nuclear field. Since April 2023, he has assumed the role of Director at the Institute for Integrated Radiation and Nuclear Science.

program opted for americium-241 (^{241}Am) instead of plutonium-238 (^{238}Pu) due to concerns about the latter's scarcity and price.[7–9]

The design of RTGs requires careful consideration of various factors, including preventing device degradation during extended service missions,[10] minimizing the total weight of the devices,[11] and using segmented TEGs to optimize output power and ensure proper operation under specific circumstances.[12–14] Furthermore, a critical aspect of RTG design is the accommodation of the TE materials for energy generation. For example, RTGs utilizing tellurium alloys must operate under an inert gas atmosphere to prevent the sublimation and oxidation of tellurium. In contrast, the SiGe based RTGs can operate without a cover gas at high temperatures (approximately 1275 K) in the space environment. Nevertheless, the oxidation of other component, typically molybdenum, presents a significant challenge to the long-term use of conventional SiGe based RTGs, requiring them to be sealed at launch on the planetary surface.[10] Given the important role of TE materials in the development of RTGs, this review presents an overview of the evolution of TE materials used in RTGs. Additionally, we explore and propose novel TE materials as promising candidates for advancing the next generation of RTGs.

2. The radioisotope thermoelectric generator (RTG)

As shown in Fig. 2, the primary components of an RTG consist of two main parts: (1) the heat source, which houses the radioisotope at the core or center of the module, and (2) the TEGs installed around the heat sources.[15] The TEGs are separated from the heat source with insulation to protect the outer components from reactions and radiation emitted by the isotope. The design and size of RTGs are determined based on mission requirements, including power consumption and mission duration. In addition, to facilitate operations at high temperatures, certain supporting components, such as cooling systems—referred to as fins—and inert gas are employed to release excess heat from the TEGs and protect the materials from oxidation.[10]

2.1. The radioisotope heat source (RHS)

Over the 1300 types of radioisotopes produced from nuclear fission reactors and particle accelerators,[16] approximately 100 are considered suitable for use as the heat source in RTGs. Given the prolonged service time of RTGs, ranging from 100 days to 100 years, the selected isotopes must meet specific criteria, including an output power requirement exceeding 0.1 W(thermal) g^{-1}. Notably, ^{238}Pu (0.39 W g^{-1}), ^{250}Cm (2.27 W g^{-1}), ^{90}Sr (0.22 W g^{-1}), and ^{241}Am (0.1 W g^{-1}) are identified as the most promising candidates. Table 1 provides a summary of the power density (W g^{-1}), half-life, and emission modes of these candidates.[16]

As illustrated in Table 1, ^{244}Cm boasts the highest thermal power output among the isotope candidates but suffers from a short half-life, with its specific heat power (W g^{-1}) halved every 18 years. In contrast, ^{90}Sr, which has a slightly longer half-life of 28 years, requires thicker shielding to protect the outer system from β-rays, thereby increasing the RTG's total weight and cost. ^{238}Pu achieves a balance by offering both a long half-life and high specific heat power from its alpha decay and is traditionally used in RTGs in the form of pure plutonium oxide (PuO$_2$).[16] However, driven by concerns regarding scarcity and cost of ^{238}Pu, the European space program has opted to use ^{241}Am, despite its lower thermal power output compared to other isotopes. This shift from ^{238}Pu to ^{241}Am is part of the European Space Agency (ESA) program since 2009 to develop new types of TEGs compatible with the power output of ^{241}Am.[8]

Due to the radioactive nature of the isotopes used in RTGs, it is essential to shield electronic components from radiation, especially gamma radiation. This protection is accomplished by employing materials such as Pt, Rh, and Pt–Rh based alloys,

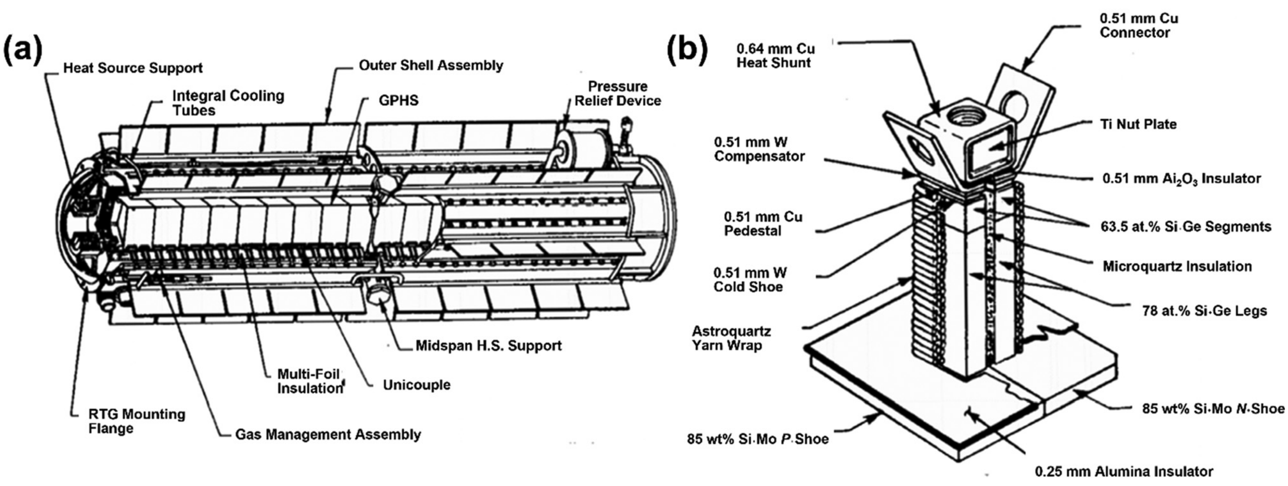

Fig. 2 (a) Illustration of a conventional RTG configuration, featuring a length of 114 cm and a diameter of 42.2 cm. The general-purpose heat source (GPHS) is located in the center of module, surrounded by TE unicouples. (b) Detailed illustration of the TE unicouple installed around the heat source. This figure is redrawn by the authors, based on the original figure.[15]

Table 1 Promising candidates of the heat source of RTG[16]

Radioisotope	Chemical forms used in RTG	Specific heat power (W g^{-1})	Half-life (year)	Emission mode
^{238}Pu	PuO_2	0.39	87.74	α
^{244}Cm	CmO_2	2.27	18.11	α
^{90}Sr	$SrTiO_2$	0.22	28.00	β
^{241}Am	AmO_2	0.1	432	α

known for their exceptional resistance to oxidation post impact,[16] to clad the radioisotope. An example of this cladding material is the platinum 20%-rhodium alloy developed by the ESA.[8,17] Surrounding the cladding, insulating and carbon–carbon composite layers are incorporated to safeguard the fuel and cladding from overheating and inadvertent incidents,[1,8] as illustrated in Fig. 3.[8] These components together constitute the radioisotope heat source (RHS) designed to endure high-velocity impacts in the event of a rocket launch failure and during Earth re-entry.

One RTG heat source design encases the radioisotopes fuel within a rectangular-shaped RHS, measuring 9.72 × 9.72 × 5.31 cm^3.[16] In this design, TEGs are mounted on the smaller surfaces of the RHS, while the larger surfaces are connected to additional RHS units. Alternatively, a six-sided polygon RHS design, as illustrated in Fig. 4,[8] keeps the major areas of the fuel element insulated, providing one surface as the interface to connect with TEGs. This innovative polygon design minimizes the volume occupied by the radioisotope, which reduces the total weight of the RTGs for use in space exploration vehicles.

2.2. Thermoelectric generator (TEG)

TEGs are mounted on the surface of the RHS, as illustrated in Fig. 2a, with numerous TE unicouples, as shown in Fig. 2b, connected in series to convert heat from the RHS into electricity. Historically, RTGs for space missions have utilized tellurium-based TE materials, notably PbTe, capable of operating within the temperature range of 300–800 K. These telluride-based TE materials have been integral to various generations of RTGs, including SNAP-3B, SNAP-9A, SNAP-19, SNAP-27, and Transit-RTG,[10] which have been widely employed in space missions to generate electricity for satellites. Notably, two SNAP-19 RTGs were used to generate 56.4 W for the Nimbus III satellite, and SNAP-27 produced 70 W during the Apollo moon missions.[18] However, the high operating temperature of PbTe necessitates the use of inert atmosphere gases, specifically argon or helium, to prevent the sublimation of TE materials. This phenomenon, typically occurring at the hot side of the TE leg, can lead to the deposition of sublimated elements on both the TE materials and electrodes, thereby reducing the TEG's efficiency.

Over time, traditional tellurium-based alloys have been supplanted by SiGe-based alloys due to their superior efficiency and higher operating temperature of 1300 K. SiGe systems exhibit enhanced thermal performance, reducing the need for extensive heat dissipation measures, which allows the use of smaller cooling fins. Additionally, the transition to multi-layered insulation from bulk insulators has effectively reduced the overall mass of RTGs. SiGe-based TEGs can also operate efficiently without the need for inert gas, enabling the removal of certain components and further reducing their total weight.[1,10] Hundreds of SiGe legs, combined with RHS modules, constitute the multi-hundred-watt radioisotope thermoelectric generators (MHW-RTG), which maintains a high power output of 150 W, diminishing to 125 W after five years of operation, with a specific power of approximately 4 W kg^{-1}. These generators have been successfully deployed in various space missions, including Voyager, where they have provided years of uninterrupted electrical power for deep solar system exploration.[10] Furthermore, advancements in SiGe-based RTGs have led to an increase in the number of TE legs from 312 to 572, paired with 18 RHSs, in the general-purpose heat source

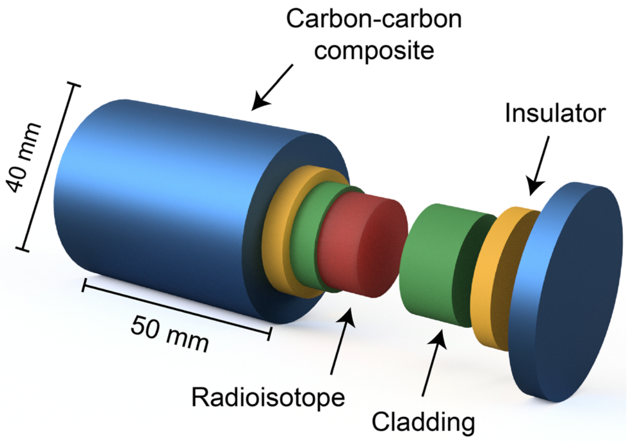

Fig. 3 The schematic depicts the configuration of the radioisotope heat source (RHS) which houses the radioisotope (red) at its core. The radioisotope is encased by cladding (green) to shield the outer parts from contamination and irradiation. Additional insulators (yellow) and carbon composite layers (blue) are strategically placed to protect the radioisotope from excessive temperatures and unforeseen accidents, respectively. This figure is redrawn by the authors based on the original figure.[8]

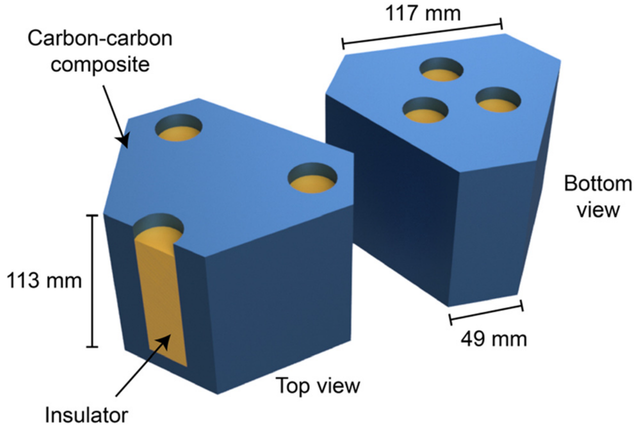

Fig. 4 The schematic diagram of the six-sided polygon-shaped RHS is depicted, where the yellow and blue areas indicate the insulating container for the radioisotope and the carbon composite material, respectively. This figure is redrawn by the authors based on the original figure.[8]

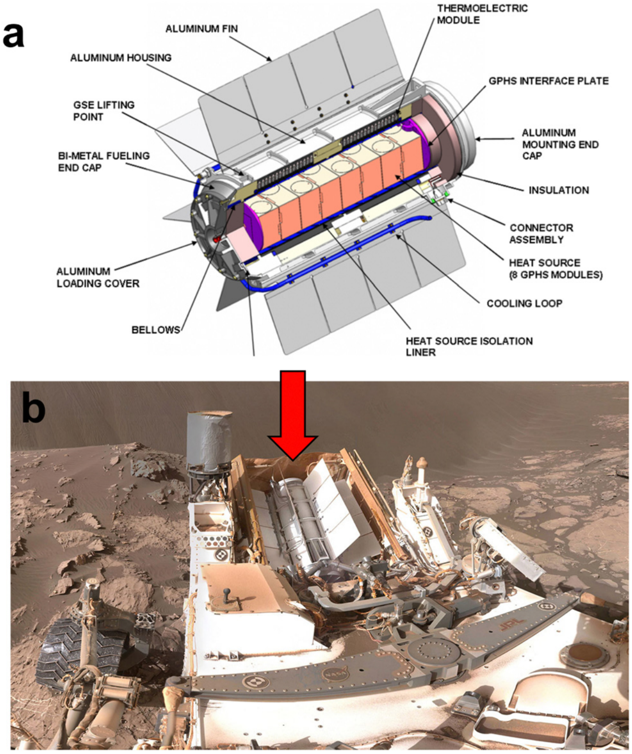

Fig. 5 (a) Configuration of the multi-mission radioisotope thermoelectric generator (MMRTG); (b) MMRTG deployed on the curiosity rover during its Mars mission. These figures were redrawn by the authors based on the original figures[21] (Image credit: NASA/JPL/Caltech).

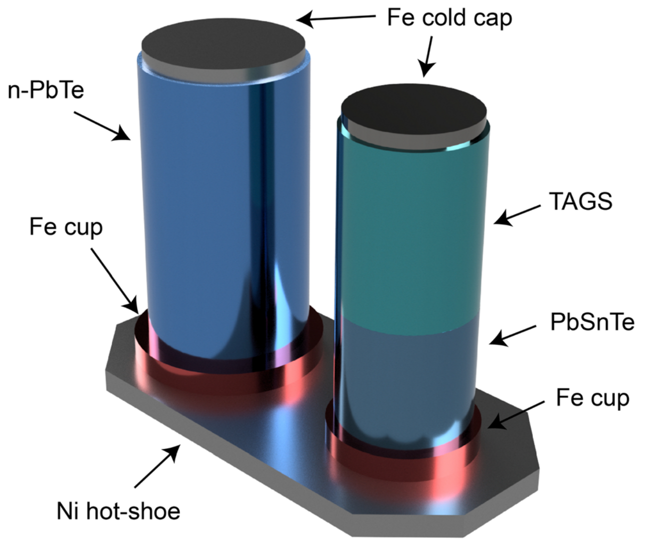

Fig. 6 Illustration of thermoelectric (TE) unicouple used in the multi-mission radioisotope thermoelectric generator (MMRTG), featuring n-type PbTe and a segmented p-type leg design. In the segmented p-type leg, PbSbTe is positioned near the hot side, while $(GeTe)_{100-x}(AgSbTe_2)_x$, known as TAGS, is placed closer to the cold side. This rendering was created by the authors based on the original figure[3] (Image credit: NASA/JPL/Caltech).

radioisotope thermoelectric generators (GPHS-RTG). This configuration achieves a higher power output of 300 W with a specific power of 5.1 W kg^{-1}.[10]

The multi-mission radioisotope power generator (MMRTG), illustrated in Fig. 5, represents the next generation of space RTGs.[19,20] Fig. 6 showcases the employment of PbTe as the n-type and $(GeTe)_{100-x}(AgSbTe_2)_x$ (TAGS)/PbSnTe as the p-type segmented TE materials in the MMRTG.[3] This innovative design enables its application across various environments, from the vacuum of space to planetary atmospheres. The MMRTG, equipped with 8 RHSs, can generate approximately 2 kW through 16 TE modules, each consisting of 48 TE unicouples. To prevent heat loss and oxidation of the TE materials, the TEG system is encased in argon gas and isolated from the RHS chamber to mitigate heat loss to the helium gas produced from fuel irradiation.[21] The expected nominal power output of MMRTG in deep space missions is 125 W at the beginning of the mission and 110 W for ground missions.[21] This power is sustained within the temperature range of 423 K to 823 K, exhibiting a specific power of 2.8 W kg^{-1}.[10] While the specific power of the MMRTG is lower than that of the SiGe-based RTGs previously discussed, it is important to note that SiGe is limited to vacuum environments, rendering them unsuited for surface missions on planets. In contrast, MMRTG's versatility allows it to generate electrical power for rovers or drones even on surface missions.

Following the success of MMRTG, its design has been recognized as reliable and highly efficient for future missions. However, given the concerns over the scarcity of ^{238}Pu, the development of a next-generation MMRTG, termed the new enhanced MMRTG (eMMRTG), is critical.[7] In eMMRTG's design, traditional TE materials are replaced with skutterudites, which are known for their exceptional TE properties and mechanical strength.[19] Unlike TAGS, whose performance deteriorates above 800 K over time due to the degradation of segmentation in p-type leg, skutterudites demonstrate high-temperature stability, allowing a hot-side operation temperature between 800 and 850 K. This higher operating temperature increases the efficiency of both n- and p-type skutterudites, thereby improving the overall efficiency of eMMRTG.[7]

Recent advancements by the ESA have led to the development of Bi_2Te_3-based TE modules, specifically designed for deep-space probes using ^{241}Am as the fuel source. These modules operate at lower hot side temperatures than those powered by ^{238}Pu,[8,9,22] enabling the use of Bi_2Te_3-based alloys as TE materials. Traditionally, Bi_2Te_3 alloys have seen limited use in RTGs due to their low operating temperature range of 300–600 K. However, their integration with ^{241}Am heat sources is highly promising. This is attributed to ^{241}Am emitting low-energy alpha and gamma radiation, which reduces the risk of introducing defects in electronic structures through irradiation. Mesalam *et al.* have demonstrated, through 10 000 hours of vacuum testing, that RTG systems incorporating these Bi_2Te_3-based modules are relatively unaffected by changes over time.[22,23] The test results indicate an annual efficiency degradation of less than 1% for these TE converters, capable of delivering a 10 W electrical power output. Future development

Table 2 Detailed information on radioisotope thermoelectric generators (RTGs) used in space missions (credit: NASA/JPL/Caltech)

RTGs		Radioisotope	TE materials	Operating temperature	Power output (W)	Scenarios	Ref.
Systems for nuclear auxiliary power (SNAP)		^{238}Pu ^{90}Sr ^{242}Cm	Telluride-based	300–800 K	28–140	Nimbus B-1 Viking 1&2 Pioneer 10&11 (Jupiter mission)	24
Example	SNAP-3B SNAP-19 SNAP-27 Transit-RTG	^{210}Po				Apollo Lunar missions	
Multi-hundred-watt radioisotope thermoelectric generators (MHW-RTG)		^{238}Pu	SiGe-based	Up to 1300 K	125–158	Voyager 1&2	
General-purpose heat source radioisotope thermoelectric generators (GPHS-RTG)					300	Galileo Cassini Ulysses New Horizons	
Multi-mission radioisotope thermoelectric generator (MMRTG)			GeTe-based, PbTe-based	400–800 K	110–125	Mars rover	21
Enhanced multi-mission radioisotope thermoelectric generator (eMMRTG)			Skutterudites	Above 800 K	25% higher than MMRTG (130–155)	Future mission	19
RTG from the European Space Agency (ESA)		^{241}Am	Bi–Te – based	300–600 K	10	Under development	25

efforts are focused on achieving a 50 W power output using the same design principles. The detailed information of the RTGs used in space missions is summarized in Table 2.

3. Thermoelectric materials for RTG

The energy conversion efficiency (ε) of RTGs typically falls within the range of 10%[1] and is determined by the following equation:

$$\varepsilon = \frac{\Delta T}{T_{\mathrm{H}}} \frac{\sqrt{1+zT-1}}{\sqrt{1+zT}+\dfrac{T_{\mathrm{C}}}{T_{\mathrm{H}}}} \quad (1)$$

here, T represents the average temperature, T_{H} and T_{C} denote the temperatures on the hot and cold sides of TEGs, respectively. ΔT is the difference between T_{H} and T_{C}, and zT is the figure of merit of the TE material. To enhance RTG's efficiency, two main approaches are considered: (1) the optimization and redesign of RTG modules, as previously discussed, and (2) the development of TE materials with zT values greater than 1, to achieve a conversion efficiency exceeding 10%. The zT values are determined by the relation:

$$zT = \frac{S^2\sigma}{\kappa}T \quad (2)$$

In this equation, S, σ and κ are the Seebeck coefficient (V K^{-1}), electrical conductivity (S m^{-1}) and total thermal conductivity (W mK^{-1}), respectively.[26] The total thermal conductivity (κ) includes contributions from both the lattice (κ_{ph}) and electronic (κ_{e}) thermal conductivities.[27]

Thermoelectric generators (TEGs) consist of pairs of n and p-type materials, characterized by negative and positive Seebeck coefficients, respectively. These pairs are usually chosen from materials with similar mechanical properties, particularly thermal expansion coefficients, to mitigate high-pressure stresses and potential damage to the TEGs at elevated temperatures.[28] Disparities in the thermal expansion coefficients of n and p-type materials can cause significant stress and damage to TEGs. It is also important to note that the same material can exhibit either n or p-type by varying the doping levels of electrons or holes. For instance, B-doped SiGe and Na-doped PbTe are classified as p-type,[29–31] while P-doped SiGe and I-doped PbTe are identified as n-type.[32]

In the preceding section, we introduced several TE materials suitable for RTG applications, including PbTe, SiGe, TAGS, Bi_2Te_3, and skutterudites. It is crucial to understand that each TE material exhibits its highest zT values at specific temperature ranges. For example, PbTe-based alloys reach their peak zT values between 600 and 900 K,[33] whereas SiGe and Bi_2Te_3 achieve their maximum zT above 1200 K[34] and within the 300 to 500 K range,[35] respectively. Therefore, aligning the thermal output of the RHS with the optimal operating temperatures of the chosen TE materials is essential for maximizing RTG efficiency. Fig. 7 illustrates the correlation between the zT value and the optimal operating temperature for various p and n-type TE materials. Moreover, operating within the optimal temperature range can reduce thermal stress generated from thermal expansion, thereby enhancing the reliability of the RTG for long-duration missions without the need for maintenance. The temperature of the RHS is controlled through several methods. Firstly, the appropriate amount of radioisotope is selected based on the specific mission requirements. Additionally, insulating and conducting materials are utilized to minimize heat loss from the RHS and to direct heat flow to the surface area of the TE materials, respectively. Adjusting these materials around the RHS can affect the amount of heat dissipated into the surroundings. Furthermore, cooling tubes and radiator fins are employed to control the temperature by removing excess heat into space.[25]

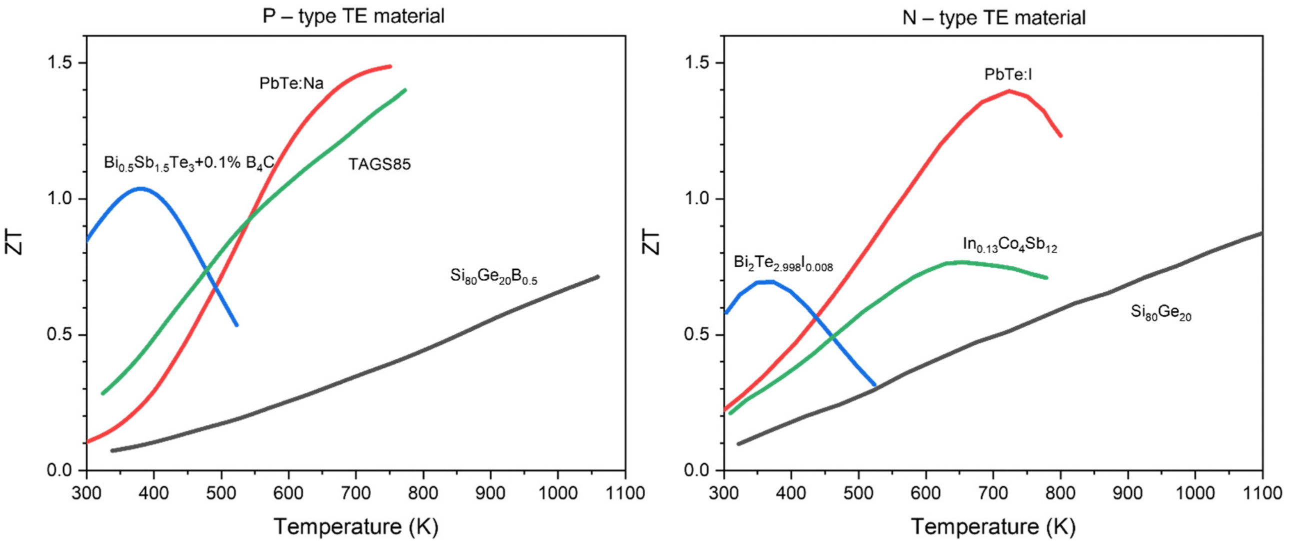

Fig. 7 Relationships between zT and optimal operating temperature ranges for selected TE materials. On the left-hand side, p-type materials include B-doped SiGe,[31] PbTe:Na,[30] $Bi_{0.5}Sn_{1.5}Te_3$ + $0.1B_4C$,[36] and TAGS85.[37] On the right-hand side, n-type materials feature SiGe,[38] PbTe:I,[32] $Bi_2Te_{2.992}I_{0.008}$,[35] In-filled $CoSb_3$.[39,40]

To achieve high zT values, it is crucial to optimize the power factor (PF), represented by the $S^2\sigma$ term in eqn (2), while also minimizing thermal conductivity. As a result, the most promising TE materials are those characterized as ''phonon-glass electron-crystal,'' which are typically semiconductors.[2] However, there is a trade-off among S, σ and κ_e, all of which are related to carrier concentration, making it challenging to optimize any single parameter without affecting the others.[2,27,41] On the other hand, κ_{ph} is the only parameter independent of carrier concentration. Therefore, the conventional approach to enhance the efficiency of TE materials involves optimizing the PF while simultaneously reducing κ_{ph}. Specifically, the addition and/or substitution of certain atoms into TE materials can manipulate the electronic band structure and reduce κ_{ph} through increased phonon-impurity scattering. Additionally, nanostructuring presents a promising strategy to achieving high zT values by scattering medium and long-wavelength phonons, without affecting electron scattering.[42]

3.1. Lead telluride alloys

Lead telluride (PbTe) features a simple, symmetrical cubic crystal structure resembling that of NaCl, with a space group of $Fm\bar{3}m$, as illustrated in Fig. 8. It is widely employed as a conventional TE material in the temperature range of 600–800 K.[43,44] Initially, PbTe was utilized in RTGs for space missions, achieving a zT of approximately 0.7 to 0.8. Advanced measurement technologies later revealed a zT of 1.4 for PbTe.[44] Despite a temporary shift to SiGe due to its need for cover gas to prevent oxidization, PbTe and its alloy PbSnTe[45–47] were eventually reintegrated into the MMRTG, as shown in Fig. 6.

In recent decades, significant efforts have been made to improve the TE properties of PbTe alloys, resulting in remarkably high zT values. These enhancement strategies fall into three broad categories:

(1) Manipulating the electronic band structure, including band convergence,[49–52] resonant states[53,54] band alignment,[55] flattened bands,[56] and deep impurity levels,[57] to achieve high PF.

(2) Optimizing carrier density by doping with I and Br at the Te site, or with Sb, Bi, Al, Ga, and In at the Pb site for n-type PbTe.[58–60] Na and P are used for doping p-type PbTe.[30,61] Noteworthy achievement include La-doped PbTe + Ag_2Te with a zT of 1.6 at 775 K,[62] $Tl_{0.02}Pb_{0.998}Te$ with a zT of 1.5 at 775 K,[54] $Pb_{0.999}TeIn_{0.001}$ with a zT of 0.85 at 623 K,[63] $Pb_{0.998}Ga_{0.02}Te$ with a zT of 1.4 at 775 K,[57] $Pb_{0.98}Ga_{0.02}Te_{0.96}Se_{0.04}$ with a zT of 1.6 at 775 K,[64] and PbTe-SrTe with a remarkable zT of 2.2 at 913 K.[51]

(3) Reducing lattice thermal conductivity by enhancing the phonon scattering from dislocations and point defects within

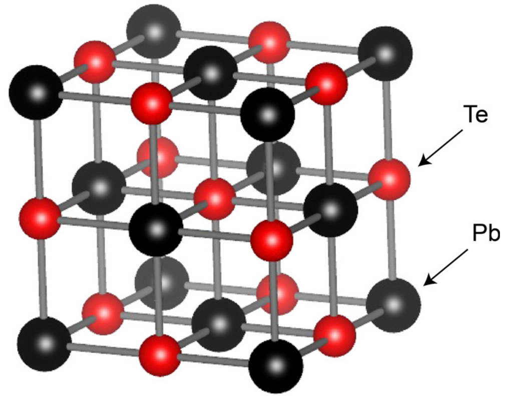

Fig. 8 Schematic of the rock-salt structure of PbTe, with black and red spheres representing Pb and Te atoms, respectively. The crystal structure information was retrieved from the Materials Project database and visualized using the VESTA software.[48]

the lattice.[60,65,66] In addition, incorporating heavy elements in Pb contributes to phonon scattering through the Umklapp process,[67] resulting in a lower κ_{ph}.[52,68,69] An example of this approach is the use of strain engineering by Wu *et al.* to reduce κ_{ph} of $Na_{0.03}Eu_{0.03}Sn_{0.02}Pb_{0.92}Te$ through in-grain dislocation, achieving a high *zT* of 2.6 at 773 K.[70]

3.2. SiGe alloys

Silicon Germanium (SiGe) alloys have been successfully utilized as TE materials in various missions, particularly for deep space exploration, due to their ability to operate in vacuum conditions without the need for cover gas. Notably, NASA used SiGe with *zT* values of 0.9 (n-type) and 0.5 (p-type) in RTGs in 1976.[71] As a Si-based alloy, SiGe exhibits a diamond crystal structure and demonstrates excellent electrical properties at temperatures above 1200 K in vacuum, attributed to its intermetallic nature. Although pure Si single crystals display high thermal conductivity, resulting in a relatively low *zT* of 0.02–0.2 at temperatures from 300 to 1200 K,[72] the substitution of Ge atoms into the Si lattice significantly enhances phonon scattering. This increase in phonon scattering reduces the lattice thermal conductivity to less than 10 W mK^{-1}, allowing SiGe to achieve a maximum *zT* more than three times higher than that of Si.

Nanostructuring techniques, such as ball milling[29,73,74] or melt spinning[31,75,76] followed by hot pressing or spark plasma sintering (SPS), have been employed to enhance the *zT* value of SiGe by reducing the grain size from single crystals to micro- and nano-grain polycrystals. These finer grains increase grain boundary scattering without negatively affecting electrical properties, thereby improving the *zT* values of SiGe to above 1.[77] The *zT* of nanostructured n-type SiGe can be further enhanced to reach approximately 1.3–1.5 at 1173 K, double that of pristine SiGe,[34,73] through carrier concentration optimizations by doping elements such as P and Sb.[34,74,78,79] For p-type SiGe, B and Ga were doped to optimize electron acceptors, yielding *zT* values between 0.5 and 1.2 at 1073 K.[29,31,79–81] In addition, nanocomposites have proven effective in reducing lattice thermal conductivity by scattering phonons. For example, integrating $Si_{80}Ge_{20}P_2$ with nano-scale silicon carbide (SiC) at 0.23 vol% significantly reduces its thermal conductivity from 2.5 to 1.9 W mK^{-1}, leading to an improved *zT* of 1.7 at 1173 K.[38] Furthermore, the incorporation of second-phase nanoinclusions of silicide (XSi_2, where X is a metallic transition element), such as VSi_2,[82] $CrSi_2$,[83] $MoSi_2$,[84] and WSi_2,[85,86] has been employed to reduce lattice thermal conductivity.[87–89] A notable example is the addition of YSi_2 to p-type SiGe, achieving a *zT* of 1.81 at 1100 K.[90] However, the stoichiometry of the composites must be carefully considered during *zT* optimization to avoid unintended changes in carrier concentrations that could lead to PF degradation and limit *zT* enhancement.

3.3. GeTe and TAGS

Germanium Telluride (GeTe) is characterized as a narrow-band gap compound with a band gap of 0.3 eV, featuring a cubic crystal structure at high temperatures and transitioning to a rhombohedral structure at lower temperatures.[91,92] It demonstrates excellent TE properties in its cubic phase and serves as a p-type TE material because of the significant amount of Ge vacancies. Consequently, strategies to enhance the *zT* of GeTe focus on manipulating the hole carrier concentration and reducing thermal conductivity.[93] For example, by substituting Sb and In atoms at the Ge site, Hong *et al.* reduced the thermal conductivity from 7 to 1 W mK^{-1} at 300 K and achieved a *zT* of 2.3 at approximately 600 K.[94] Li *et al.* successfully reduced the thermal conductivity to 0.7 and achieved a *zT* of 2.4 at 600 K by substituting Pb and Bi atoms at the Ge site.[95] Tsai *et al.* suppressed the thermal conductivity of GeTe by alloying with Sb_2Te_3, inducing the coexistence of cubic and rhombohedral GeTe phases. This resulted in a *zT* of 2.5–2.9 at 720 K for $(GeTe)_{0.95}(Sb_2Te_3)_{0.05}$.[96] Moreover, Bu *et al.* coalloyed GeTe with Cu_2Te and PbSe to simultaneously optimize the carrier concentration, suppress the lattice thermal conductivity, and maintain a relatively high carrier mobility in p-type $(Ge_{0.98}Cu_{0.04}Te)_{1-y}(PbSe)_y$ alloys. This approach resulted in a maximum *zT* value of over 2.5 at 800 K and an average *zT* of 1.8 between 300 and 800 K.[97] The solid solution of GeTe and $AgSbTe_2$, known as TAGS, is well-recognized for its high *zT* in the mid-temperature range (600 to 800 K) and for its mechanical stability at operating temperatures.[98] Efforts dedicated to enhancing the *zT* of TAGS include doping with rare earth elements,[99,100] optimizing the stoichiometry of GeTe–$AgSbTe_2$ and vacancies,[37,101] substituting variants elements,[102–104] and microstructure engineering.[105,106] Notably, Rodenkirchen *et al.* reported a high *zT* of 1.8 at 750 K and an average *zT* of 1.37 in the range of 300 to 800 K for TAGS.[105]

As illustrated in Fig. 6, TAGS is employed in MMRTG, along with PbSnTe, as the p-type TE materials in the segmented design. The performance of the segmented TE leg increases when the two TE materials are compatible, and compatibility factor ($\dot{s}$), is determined using the equation:

$$\dot{s} = \frac{\sqrt{1 + zT} - 1}{S \cdot T} \tag{3}$$

It is crucial that the compatibility factor do not differ by a factor greater than two,[12,14,107] as this discrepancy can significantly reduce the overall efficiency of TEGs.[14] As illustrated in Fig. 9, TAGS-85[37] and PbSnTe[47] exhibit excellent compatibility with each other between 300 to 600 K, which led to their selection as the p-type segmented legs for the MMRTG. However, compatibility is just one of several factors to be considered in selecting TE materials for TEGs that utilize segmented designs. Potential incompatibility may emerge from the degradation of segmented TE materials over the course of the mission, especially due to irradiation effects.[108] Therefore, it is essential to consider other properties of the TE materials, such as thermal expansion coefficient, interdiffusion rates, mechanical properties, and resistance to irradiation, to ensure the durability of the RTGs.

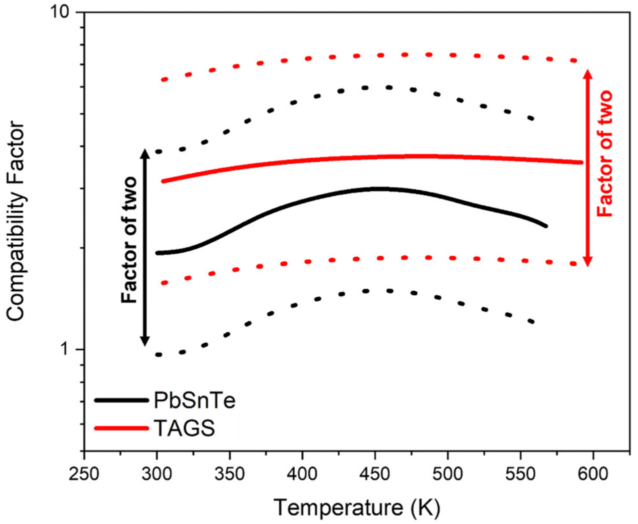

Fig. 9 The compatibility factors of TAGS[37] and PbSnTe[47] in the p-type legs of the multi-mission radioisotope thermoelectric generator (MMRTG). The bold and dotted lines represent the compatibility factors calculated based on eqn (3) and the compatible range of a factor of two, respectively.

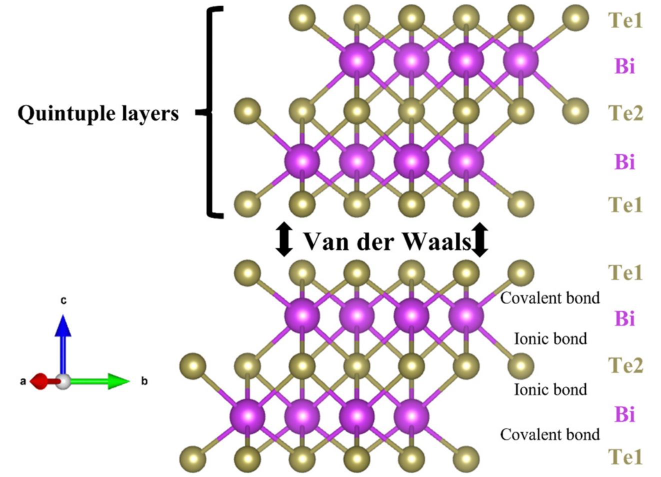

Fig. 10 Bi_2Te_3 exhibits a rhombohedral structure consisting of quintuple layers, Te1–Bi–Te2–Bi–Te1, connected by van der Waals bonding along the *c*-axis. Information on the crystal structure was sourced from materialproject.org and visually represented using VESTA.[48]

3.4. Bi_2Te_3-based alloys

Bi_2Te_3 crystallizes in a rhombohedral structure, featuring quintuple-layers of Te1–Bi–Te2–Bi–Te1 separated by van der Waals bonding along the *c*-axis, as indicated in Fig. 10.[109] The Te2–Bi bonds are longer, indicative of ionic bonding, while the Te1–Bi bonds are shorter, suggesting covalent bonding. The anisotropy in the microstructure and the relatively weak van der Waals bonding along the *c*-axis contribute to distinct TE properties between the *a*,*b* axis and *c*-axis. At room temperature, the bandgap of Bi_2Te_3 is measured at 0.13 eV.[110]

Current strategies to enhance the TE properties of Bi_2Te_3 include nanostructuring and alloying. For instance, nanostructuring Bi_2Te_3 with SnTe through ball milling and hot pressing reduced its thermal conductivity from 1.4 to 0.9 W mK^{-1} at 373 K, achieving a zT value of 1.4.[111] Additionally, synthesizing multiscale microstructures through melt-spinning and SPS in $(Bi,Sb)_2Te_3$ can also significantly lower thermal conductivity while preserving electrical properties, resulting in a zT of 1.5 at 390 K.[112] Xu *et al.* utilized SPS to prepare highly porous $Bi_2Te_{2.5}Se_{0.5}$ nanocomposites from hollow nanorods, achieving an ultralow lattice thermal conductivity of 0.13 W mK^{-1} and a zT of over 1 between 388 and 513 K.[113] Another approach involves the use of excess Te in the melting process, which is released during sintering to create dense dislocation arrays at low-energy grain boundaries, scattering mid-wavelength phonons and yielding a zT of 1.81 at 350 K.[114] The introduction of SiC nanoprecipitates into Bi_2Te_3 has also been explored to enhance its electrical conductivity and the Seebeck coefficient through increasing carrier concentration. SiC nanoprecipitates effectively scatter low-energy electrons without adversely affecting electrical conductivity, a phenomenon termed 'energy filtering'. Despite a slight increase in thermal conductivity due to enhanced electron heat transport, a high zT of 1.33 at 373 K has been reported, underscoring the success of this approach[115,116] Notably, the addition of SiC not only improves the TE properties of Bi_2Te_3 but also enhances its hardness. Finally, various doping strategies aimed to enhance the TE properties of Bi_2Te_3, such as Cu-doped Bi_2Te_3 (zT = 0.67 at 415 K),[117] $Ce_{0.2}Bi_{1.8}Te_3$ (zT = 1.29 at 398 K),[118] and $Bi_{2-x}Ge_xTe_3$ (zT = 0.95 at 300 K)[119] have been extensively reviewed by Saberi and Sajjadi, respectively.[120]

Bi_2Te_3, recognized for its outstanding TE properties, was originally employed as a cooling TE material, capable of generating a temperature difference of 40 K at room temperature.[121] However, its application in RTGs for space missions has been limited due to its incompatibility with the operating temperature of ^{238}Pu RHS and a low melting point at 858 K.[110] Following the shift by the ESA to replace ^{238}Pu with ^{241}Am, Bi_2Te_3 was later adopted for their space missions.[8] Given that ^{241}Am emits alpha particles and slight gamma-rays, evaluating the irradiation resistance of Bi_2Te_3 TEGs is crucial to ensure their structural integrity during missions. A report by Mesalam *et al.* revealed the ratio between post- and pre-irradiation zT values ranges from 0.7 to 1.2. Various trends in zT after irradiation in the literature are attributed to the effect of irradiation on the TE material's atomic structure, leading to the formation of vacancies and interstitials, thereby impacting carrier concentration, σ and S values.[22,122]

3.5. Skutterudites ($CoSb_3$)

Skutterudite, a $CoSb_3$-based alloy, crystallizes into a cubic crystal structure characterized by octahedrons within the $Im\bar{3}$ space group, as illustrated in Fig. 11. This structure features a void at the center of the lattice that can accommodate specific atoms, enhancing phonon scattering and thereby improving electrical properties. As a narrow bandgap semiconductor (0.22 eV), $CoSb_3$ exhibits high carrier concentration and excellent electrical conductivity. Additionally, it possesses a high Seebeck coefficient due to its flat energy band.[39] The presence of a covalent bond between Co and Sb, coupled with a high void density in the structure, leads to a high thermal conductivity of approximately 10 W mK^{-1} for a single crystal,[123] resulting in a low *zT*.[39] To enhance the thermal conductivity of skutterudites, one effective strategy involves the substitution of atoms at the Co or Sb sites. For instance, doping Te on the Sb site not only reduces thermal conductivity but also acts as an electron donor to improve electrical properties, achieving a *zT* of 0.93 at 800 K.[124] Similarly, Ni doping at the Co site effectively reduces thermal conductivity from 11 to 6 W mK^{-1} at room temperature.[125] Binary substitution at both the Co and Sb sites, as in the case of $Co_{1-x}Ni_x(Sb_{1-y}Te_y)_3$, yields a *zT* of 0.65 at 800 K.[126] Furthermore, co-doping of Ge and Te at the Sb site, aimed at increasing Te solubility and enhancing point defect scattering, has resulted in a high *zT* of 1.1 at 800 K.[127] Another notable approach intended to reduce thermal conductivity involves the introduction of filling atoms into the voids in the microstructure. For instance, Zhang *et al.* incorporated Li as filling atom to effective scatter phonons. The optimized composition of Li-filled $CoSb_3$, $Li_{0.36}Co_4Sb_{12}$, demonstrated a high and stable PF value of 6 mW mK^{-2} from room temperature to 700 K, along with an excellent *zT* of 1.3 at 700 K.[128]

However, relying solely on single-element filling or substitution proves inadequate for maximizing the TE properties of $CoSb_3$. Sales *et al.* introduced the concept of using multiple filler atoms, La and Ce, in combination with Fe substitution at the Co-site. This strategy significantly reduced the thermal conductivity from 10 to 1.6 W mK^{-1} at room temperature and achieved a *zT* of 0.9 at 800 K.[129] A co-doping approach using Dy and Ni, optimized to $Dy_{0.4}Co_{3.2}Ni_{0.8}Sb_{12}$, exhibited a high *zT* of 1.4 at 773 K, with the Ni doping also enhancing the mechanical properties.[130] Furthermore, Shi *et al.* achieved a high *zT* of 1.7 at 850 K using multiple filler atoms, such as Ba, La, and Yb, in $CoSb_3$.[131] Nanostructuring of $CoSb_3$ has also been explored to enhance its TE properties, where specific nano grain sizes scatter phonons at the grain boundaries. For instance, Rogl *et al.* synthesized the triple-filled skutterudite $(Sr_{0.33}Ba_{0.33}Yb_{0.33})_{0.35}Co_4Sb_{12.3}$ using ball milling and hot-pressing techniques, achieving a PF of 6 mW mK^{-2} and a *zT* of 1.4 at 823 K. Subsequently, the $(Sr_{0.25}Ba_{0.25}Yb_{0.5})_{0.5}Co_4Sb_{12.5}$ sample, incorporating homogeneous nanosized Yb_2O_3 impurities, exhibited a *zT* of 1.6 at 835 K. High-pressure torsion was applied to further reduce its thermal conductivity, resulting in an enhanced *zT* of 1.9 at 835 K.[132] Additionally, melt-spinning followed by SPS was utilized to prepare nanostructured (In, Ce)$CoSb_3$ nanocomposites, incorporating a wide range of nanoparticles to strongly scatter phonons and achieve a *zT* of 1.5 at 850 K.[133]

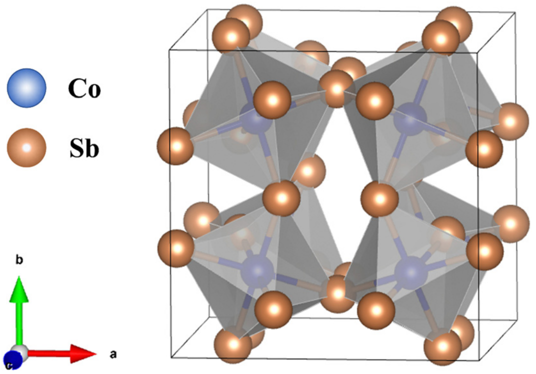

Fig. 11 Illustration of the crystal structure of the $CoSb_3$-based alloy, which crystallizes into octahedrons within the space group $Im\bar{3}$. The structure is characterized by a void at the center of the cubic lattice. Crystal structure information was sourced from materialproject.org and visually represented using VESTA.[48]

4. Practical usage

The optimization and design of TEGs and RHSs are critical in enhancing the electrical energy output of RTGs. Beyond TE properties, various factors must be considered prior to the selection and assembly of RTGs for practical use. These factors include the stability of TE materials at operating temperatures and their resistance to irradiation, both of which are essential for mitigating RTG degradation during missions. A significant issue concerning stability is the sublimation of chalcogen elements, such as Te and Se, which are primary components in most TE materials. Sublimation can result in numerous problems, such as a reduction in the TE leg's cross-sectional area, an increase in electrical and thermal resistance, and possible impacts on the junction between TE materials and electrodes, potentially resulting in system failure. Although sublimation cannot be entirely prevented, it can be delayed through the use of cover gases and/or coatings on TE legs.[1] Additionally, the high operating temperature may facilitate interdiffusion between the TE material and the electrode bonding material, potentially reducing TE performance.[134,135] Consequently, a diffusion barrier should be installed between the TE legs and the electrodes to inhibit the formation of secondary phases.[136] Moreover, the high operating temperature, large temperature differences between the hot and cold sides, and mismatch in thermal expansion coefficients between the p- and n-type TE legs can induce substantial internal stresses, risking long-term RTG failure. To enhance structural integrity, TE couples should be selected to minimize difference in thermal expansion coefficients, and optimization of the surface area and length of n- and p-type TE legs can help mitigate these stresses.[137] Finally, while this review has primarily focused on large-scale RTGs used in space explorations, RTGs with smaller sizes and lower power outputs also hold promise for niche applications, such as powering remote sensors or implantable medical devices like pacemakers.[138–140] However, significant efforts are required to advance the use of micro-RTGs, as challenges remain in the fabrication of small-scale TE modules on the order of centimeters and ensuring effective contact between the miniaturized heat sources and TE couples.[141] Moreover, as micro-RTGs will operate at significantly lower power outputs and temperatures compared to their space exploration counterparts, developing TE materials with optimal zT values at low to intermediate temperatures remains critical.

5. Conclusion

This review presents a comprehensive examination of the evolution of RTGs over the past fifty years, alongside prospects for future missions. It offers an in-depth analysis of the meticulous selection of RHSs and TE materials across different RTG generations. The discussion delves into the TE properties of conventional materials used in RTGs and explores promising techniques to enhance these properties. A key focus of this review is the enhancement of zT through two fundamental principles: increasing the PF by optimizing the electronic band structure and reducing κ by increasing phonon scattering. While the ongoing development of TE materials with high zT is crucial to advancements in RTG design, these materials must also meet other criteria essential for RTG integration, such as strength, safety, and weight considerations. Moreover, the authors emphasize the importance of prioritizing safety in RTG design for future space travels, aligning with humanity's broader aspirations. This perspective underscores the need for RTGs to incorporate enhanced safety measures to safeguard human well-being during space exploration in the foreseeable future.

Conflicts of interest

There are no conflicts to declare.

Acknowledgements

This work was supported in part by MEXT/JSPS KAKENHI, grant number 24K08029.

References

1 C. Candolfi, S. E. Oualid, D. Ibrahim, S. Misra, O. E. Hamouli, A. Léon, A. Dauscher, P. Masschelein, P. Gall, P. Gougeon, C. Semprimoschnig and B. Lenoir, *CEAS Space J.*, 2021, **13**, 325–340.
2 G. J. Snyder and E. S. Toberer, *Nat. Mater.*, 2008, **7**, 105.
3 R. Cataldo and G. Bennett, U.S. Space Radioisotope Power Systems and Applications, *Past, Present and Future*, 2011, DOI: 10.5772/23914.
4 M. L. Terranova, *Int. J. Energy Res.*, 2022, **46**, 19368–19393.
5 M. A. Zoui, S. Bentouba, J. G. Stocholm and M. Bourouis, *Energies*, 2020, **13**, 3606.
6 G. Bennett, in *4th International Energy Conversion Engineering Conference and Exhibit (IECEC)*, DOI: 10.2514/6.2006-4191.
7 T. C. Holgate, R. Bennett, T. Hammel, T. Caillat, S. Keyser and B. Sievers, *J. Electron. Mater.*, 2015, **44**, 1814–1821.
8 R. M. Ambrosi, H. Williams, E. J. Watkinson, A. Barco, R. Mesalam, T. Crawford, C. Bicknell, P. Samara-Ratna, D. Vernon, N. Bannister, D. Ross, J. Sykes, M.-C. Perkinson, C. Burgess, C. Stroud, S. Gibson, A. Godfrey, R. G. Slater, M. J. Reece, K. Chen, K. Simpson, R. Tuley, M. Sarsfield, T. P. Tinsley, K. Stephenson, D. Freis, J.-F. Vigier, R. J. M. Konings, C. Fongarland, M. Libessart, J. Merrifield, D. P. Kramer, J. Byrne and B. Foxcroft, *Space Sci. Rev.*, 2019, **215**, 55.
9 H. R. Williams, R. M. Ambrosi, N. P. Bannister, P. Samara-Ratna and J. Sykes, *Int. J. Energy Res.*, 2012, **36**, 1192–1200.
10 J. Yang and T. Caillat, *MRS Bull.*, 2006, **31**, 224–229.
11 X. Hu, P. Jood, M. Ohta, M. Kunii, K. Nagase, H. Nishiate, M. G. Kanatzidis and A. Yamamoto, *Energy Environ. Sci.*, 2016, **9**, 517–529.
12 C. Hadjistassou, E. Kyriakides and J. Georgiou, *Energy Convers. Manage.*, 2013, **66**, 165–172.
13 C. S. R. Matthes, D. F. Woerner, T. J. Hendricks, J. Fleurial, K. I. Oxnevad, C. D. Barklay and J. F. Zakrajsek, 2018, IEEE Aerospace Conference, Big Sky, MT, USA, 2018, pp. 1–9, DOI: 10.1109/AERO.2018.8396738.
14 G. J. Snyder, *Appl. Phys. Lett.*, 2004, **84**, 2436–2438.
15 N. Jaziri, A. Boughamoura, J. Müller, B. Mezghani, F. Tounsi and M. Ismail, *Energy Rep.*, 2020, **6**, 264–287.
16 A. Sanchez-Torres, *Radioisotope Power Systems for Space Applications*, 2011, DOI: 10.5772/20928.
17 H. Inouye, C. T. Liu and R. G. Donnelly, *New Platinum–Rhodium–Tungsten Alloys for Space Isotopic Heat Sources*, Oak Ridge National Laboratory, United States, 1972.
18 J. R. Bates, W. W. Lauderdale and H. Kernaghan, *ALSEP Termination Report*, NASA, 1979.
19 D. Woerner, *J. Electron. Mater.*, 2016, **45**, 1278–1283.
20 C. Barklay, D. Kramer, C. Whiting, R. Ambrosi and R. Mesalam, 2020 IEEE Aerospace Conference, Big Sky, MT, USA, 2020, pp. 1–7, DOI: 10.1109/AERO47225.2020.9172602.
21 T. Hammel, R. Bennett, W. Otting and S. Fanale, in *7th International Energy Conversion Engineering Conference*, 2009, DOI: 10.2514/6.2009-4576.
22 R. Mesalam, H. R. Williams, R. M. Ambrosi, D. P. Kramer, C. D. Barklay, J. García-Cañadas, K. Stephenson and D. P. Weston, *AIP Adv.*, 2019, **9**, 055006.
23 R. Mesalam, H. R. Williams, R. M. Ambrosi, J. García-Cañadas and K. Stephenson, *Appl. Energy*, 2018, **226**, 1208–1218.
24 NASA, Powering Radioisotope Thermoelectric Generators (RTGs), https://science.nasa.gov/planetary-science/programs/radioisotope-power-systems/power-radioisotope-thermoelectric-generators/#hds-sidebar-nav-1).
25 R. M. Ambrosi, H. Williams, E. J. Watkinson, A. Barco, R. Mesalam, T. Crawford, C. Bicknell, P. Samara-Ratna, D. Vernon, N. Bannister, D. Ross, J. Sykes, M.-C. Perkinson, C. Burgess, C. Stroud, S. Gibson, A. Godfrey, R. G. Slater, M. J. Reece, K. Chen, K. Simpson, R. Tuley, M. Sarsfield, T. P. Tinsley, K. Stephenson, D. Freis, J.-F. Vigier, R. J. M. Konings, C. Fongarland, M. Libessart, J. Merrifield, D. P. Kramer, J. Byrne and B. Foxcroft, *Space Sci. Rev.*, 2019, **215**, 55.
26 X.-L. Shi, J. Zou and Z.-G. Chen, *Chem. Rev.*, 2020, **120**, 7399–7515.

27 J. R. Sootsman, D. Y. Chung and M. G. Kanatzidis, *Angew. Chem., Int. Ed.*, 2009, **48**, 8616.

28 L. Pavlova, Y. Shtern and E. Kirilenko, *J. Mater. Sci.*, 2017, **52**, 921–934.

29 G. Joshi, H. Lee, Y. Lan, X. Wang, G. Zhu, D. Wang, R. W. Gould, D. C. Cuff, M. Y. Tang, M. S. Dresselhaus, G. Chen and Z. Ren, *Nano Lett.*, 2008, **8**, 4670–4674.

30 Y. Pei, A. LaLonde, S. Iwanaga and G. J. Snyder, *Energy Environ. Sci.*, 2011, **4**, 2085–2089.

31 S. Wongprakarn, S. Pinitsoontorn, S.-A. Tanusilp and K. Kurosaki, *Mater. Sci. Semicond. Process.*, 2018, **88**, 239–249.

32 A. D. LaLonde, Y. Pei and G. J. Snyder, *Energy Environ. Sci.*, 2011, **4**, 2090–2096.

33 T. Fu, X. Yue, H. Wu, C. Fu, T. Zhu, X. Liu, L. Hu, P. Ying, J. He and X. Zhao, *J. Materiomics*, 2016, **2**, 141–149.

34 X. W. Wang, H. Lee, Y. C. Lan, G. H. Zhu, G. Joshi, D. Z. Wang, J. Yang, A. J. Muto, M. Y. Tang, J. Klatsky, S. Song, S. M. Dresselhaus, G. Chen and Z. F. Gen, *Appl. Phys. Lett.*, 2008, **93**, 193121.

35 I. T. Witting, T. C. Chasapis, F. Ricci, M. Peters, N. A. Heinz, G. Hautier and G. J. Snyder, *Adv. Electron. Mater.*, 2019, **5**, 1800904.

36 H. R. Williams, R. M. Ambrosi, K. Chen, U. Friedman, H. Ning, M. J. Reece, M. C. Robbins, K. Simpson and K. Stephenson, *J. Alloys Compd.*, 2015, **626**, 368–374.

37 T. Schröder, T. Rosenthal, N. Giesbrecht, M. Nentwig, S. Maier, H. Wang, G. J. Snyder and O. Oeckler, *Inorg. Chem.*, 2014, **53**, 7722–7729.

38 S. Bathula, M. Jayasimhadri, B. Gahtori, A. Kumar, A. K. Srivastava and A. Dhar, *Phys. Chem. Chem. Phys.*, 2017, **19**, 25180–25185.

39 Z.-Y. Liu, J.-L. Zhu, X. Tong, S. Niu and W.-Y. Zhao, *J. Adv. Ceram.*, 2020, **9**, 647–673.

40 S. Le Tonquesse, É. Alleno, V. Demange, V. Dorcet, L. Joanny, C. Prestipino, O. Rouleau and M. Pasturel, *J. Alloys Compd.*, 2019, **796**, 176–184.

41 T. M. Tritt and M. A. Subramanian, *MRS Bull.*, 2006, **31**, 188.

42 M. G. Kanatzidis, *Chem. Mater.*, 2010, **22**, 648–659.

43 Y. Xiao and L.-D. Zhao, *npj Quantum Mater.*, 2018, **3**, 55.

44 A. D. LaLonde, Y. Pei, H. Wang and G. Jeffrey Snyder, *Mater. Today*, 2011, **14**, 526–532.

45 A. D. Lalonde and P. D. Moran, *J. Electron. Mater.*, 2010, **39**, 8–14.

46 V. Jovovic, S. J. Thiagarajan, J. P. Heremans, T. Komissarova, D. Khokhlov and A. Nicorici, *J. Appl. Phys.*, 2008, **103**(5), 053710.

47 A. D. Lalonde and P. D. Moran, *J. Electron. Mater.*, 2010, **39**, 8–14.

48 K. Momma and F. Izumi, *J. Appl. Crystallogr.*, 2011, **44**, 1272–1276.

49 Y. Pei, X. Shi, A. LaLonde, H. Wang, L. Chen and G. J. Snyder, *Nature*, 2011, **473**, 66–69.

50 L. D. Zhao, H. J. Wu, S. Q. Hao, C. I. Wu, X. Y. Zhou, K. Biswas, J. Q. He, T. P. Hogan, C. Uher, C. Wolverton, V. P. Dravid and M. G. Kanatzidis, *Energy Environ. Sci.*, 2013, **6**, 3346–3355.

51 K. Biswas, J. He, I. D. Blum, C.-I. Wu, T. P. Hogan, D. N. Seidman, V. P. Dravid and M. G. Kanatzidis, *Nature*, 2012, **489**, 414–418.

52 G. Tan, F. Shi, S. Hao, L.-D. Zhao, H. Chi, X. Zhang, C. Uher, C. Wolverton, V. P. Dravid and M. G. Kanatzidis, *Nat. Commun.*, 2016, **7**, 12167.

53 J. P. Heremans, B. Wiendlocha and A. M. Chamoire, *Energy Environ. Sci.*, 2012, **5**, 5510–5530.

54 J. P. Heremans, V. Jovovic, E. S. Toberer, A. Saramat, K. Kurosaki, A. Charoenphakdee, S. Yamanaka and G. J. Snyder, *Science*, 2008, **321**, 554–557.

55 K. Biswas, J. He, Q. Zhang, G. Wang, C. Uher, V. P. Dravid and M. G. Kanatzidis, *Nat. Chem.*, 2011, **3**, 160–166.

56 Y. Xiao, H. Wu, J. Cui, D. Wang, L. Fu, Y. Zhang, Y. Chen, J. He, S. J. Pennycook and L.-D. Zhao, *Energy Environ. Sci.*, 2018, **11**, 2486–2495.

57 X. Su, S. Hao, T. P. Bailey, S. Wang, I. Hadar, G. Tan, T.-B. Song, Q. Zhang, C. Uher, C. Wolverton, X. Tang and M. G. Kanatzidis, *Adv. Energy Mater.*, 2018, **8**, 1800659.

58 L. Fu, M. Yin, D. Wu, W. Li, D. Feng, L. Huang and J. He, *Energy Environ. Sci.*, 2017, **10**, 2030–2040.

59 J. Zhang, D. Wu, D. He, D. Feng, M. Yin, X. Qin and J. He, *Adv. Mater.*, 2017, **29**, 1703148.

60 Q. Zhang, Q. Song, X. Wang, J. Sun, Q. Zhu, K. Dahal, X. Lin, F. Cao, J. Zhou, S. Chen, G. Chen, J. Mao and Z. Ren, *Energy Environ. Sci.*, 2018, **11**, 933–940.

61 Q. Zhang, F. Cao, W. Liu, K. Lukas, B. Yu, S. Chen, C. Opeil, D. Broido, G. Chen and Z. Ren, *J. Am. Chem. Soc.*, 2012, **134**, 10031–10038.

62 Y. Pei, J. Lensch-Falk, E. S. Toberer, D. L. Medlin and G. J. Snyder, *Adv. Funct. Mater.*, 2011, **21**, 241–249.

63 T. Parashchuk, Z. Dashevsky and K. Wojciechowski, *J. Appl. Phys.*, 2019, **125**, 245103.

64 Y. Shi, Y. Tang, K. Liu, S. Zhong, S. Chen, L. Yu, J. Wu, Q. Zhang, X. Su and X. Tang, *Mater. Today Phys.*, 2022, **27**, 100766.

65 J. He, S. N. Girard, M. G. Kanatzidis and V. P. Dravid, *Adv. Funct. Mater.*, 2010, **20**, 764–772.

66 R. Knura, T. Parashchuk, A. Yoshiasa and K. T. Wojciechowski, *Dalton Trans.*, 2021, **50**, 4323–4334.

67 C. Chang and L.-D. Zhao, *Mater. Today Phys.*, 2018, **4**, 50–57.

68 O. Delaire, J. Ma, K. Marty, A. F. May, M. A. McGuire, M. H. Du, D. J. Singh, A. Podlesnyak, G. Ehlers, M. D. Lumsden and B. C. Sales, *Nat. Mater.*, 2011, **10**, 614–619.

69 D. M. Rowe and C. M. Bhandari, *Appl. Phys. Lett.*, 1985, **47**, 255–257.

70 Y. Wu, Z. Chen, P. Nan, F. Xiong, S. Lin, X. Zhang, Y. Chen, L. Chen, B. Ge and Y. Pei, *Joule*, 2019, **3**, 1276–1288.

71 B. Yu, M. Zebarjadi, H. Wang, K. Lukas, H. Wang, D. Wang, C. Opeil, M. S. Dresselhaus, G. Chen and Z. F. Ren, *Nano Lett.*, 2012, **12**, 2077.

72 S. K. Bux, R. G. Blair, P. K. Gogna, H. Lee, G. Chen, M. S. Dresselhaus, R. B. Kaner and J. Fleurial, *Adv. Funct. Mater.*, 2009, **19**, 2445.

73 S. Bathula, M. Jayasimhadri, N. Singh, A. K. Srivastava, J. Pulikkotil, A. Dhar and R. C. Budhani, *Appl. Phys. Lett.*, 2012, **101**, 213902.

74 S. Bathula, M. Jayasimhadri, A. Dhar, M. Saravanan, D. K. Misra, N. Singh, A. K. Srivastava and R. C. Budhani, *MRS Online Proceedings Library*, 2012, vol. 1490, pp. 74–79.

75 A. Vishwakarma, N. S. Chauhan, R. Bhardwaj, K. K. Johari, S. R. Dhakate, B. Gahtori and S. Bathula, *J. Electron. Mater.*, 2021, **50**, 364–374.

76 S. Wongprakarn, S. Pinitsoontorn, S.-A. Tanusilp and K. Kurosaki, *Phys. Status Solidi A*, 2017, **214**, 1700235.

77 G. H. Zhu, H. Lee, Y. C. Lan, X. W. Wang, G. Joshi, D. Z. Wang, J. Yang, D. Vashaee, H. Guilbert, A. Pillitteri, M. S. Dresselhaus, G. Chen and Z. F. Ren, *Phys. Rev. Lett.*, 2009, **102**, 196803.

78 C. Wang, S. Lin, H. Chen, Y. Zhao, L. Zhao, H. Wang, D. Huo and X. Chen, *Energy Convers. Manage.*, 2015, **94**, 331–336.

79 J. P. Fleurial, J. Vandersande, N. Scoville, C. Bajgar and J. Beaty, *AIP Conf. Proc.*, 1993, **271**, 759–764.

80 S. Bathula, M. Jayasimhadri, B. Gahtori, N. K. Singh, K. Tyagi, A. K. Srivastava and A. Dhar, *Nanoscale*, 2015, **7**, 12474–12483.

81 S. Lin, C. Wang, H. Chen, D. Huo, N. Savvides and X. Chen, *Funct. Mater. Lett.*, 2014, **07**, 1450008.

82 S. Tanusilp, K. Kurosaki, A. Yusufu, Y. Ohishi, H. Muta and S. Yamanaka, *J. Electron. Mater.*, 2017, **46**, 3249.

83 Z. Zamanipour and D. Vashaee, *J. Appl. Phys.*, 2012, **112**, 093714.

84 K. Favier, G. Bernard-Granger, C. Navone, M. Soulier, M. Boidot, J. Leforestier, J. Simon, J.-C. Tedenac and D. Ravot, *Acta Mater.*, 2014, **64**, 429–442.

85 J. Mackey, F. Dynys and A. Sehirlioglu, *Acta Mater.*, 2015, **98**, 263–274.

86 F. W. Dynys, A. Sayir, J. Mackey and A. Sehirlioglu, *J. Alloys Compd.*, 2014, **604**, 196–203.

87 N. Mingo, D. Hauser, P. N. Kobayashi, M. Plissonnier and A. Shakouri, *Nano Lett.*, 2009, **9**, 711.

88 K. Kurosaki, A. Yusufu, Y. Miyazaki, Y. Ohishi, H. Muta and S. Yamanaka, *Mater. Trans.*, 2016, **57**, 1018.

89 A. Nozariasbmarz, A. Agarwal, Z. A. Coutant, M. J. Hall, J. Liu, R. Liu, A. Malhortra and P. Norouzzadeh, *Jpn. J. Appl. Phys.*, 2017, **56**, 05DA04.

90 S. Ahmad, A. Singh, A. Bohra, R. Basu, S. Bhattacharya, R. Bhatt, K. N. Meshram, M. Roy, S. K. Sarkar, Y. Hayakawa, A. K. Debnath, D. K. Aswal and S. K. Gupta, *Nano Energy*, 2016, **27**, 282–297.

91 Y. Gelbstein, J. Davidow, E. Leshem, O. Pinshow and S. Moisa, *Phys. Status Solidi B*, 2014, **251**, 1431–1437.

92 X. Zhang, Z. Bu, S. Lin, Z. Chen, W. Li and Y. Pei, *Joule*, 2020, **4**, 986–1003.

93 E. M. Levin, M. F. Besser and R. Hanus, *J. Appl. Phys.*, 2013, **114**, 083713.

94 M. Hong, Z.-G. Chen, L. Yang, Y.-C. Zou, M. S. Dargusch, H. Wang and J. Zou, *Adv. Mater.*, 2018, **30**, 1705942.

95 J. Li, X. Zhang, Z. Chen, S. Lin, W. Li, J. Shen, I. T. Witting, A. Faghaninia, Y. Chen, A. Jain, L. Chen, G. J. Snyder and Y. Pei, *Joule*, 2018, **2**, 976–987.

96 Y.-F. Tsai, P.-C. Wei, L. Chang, K.-K. Wang, C.-C. Yang, Y.-C. Lai, C.-R. Hsing, C.-M. Wei, J. He, G. J. Snyder and H.-J. Wu, *Adv. Mater.*, 2021, **33**, 2005612.

97 Z. Bu, X. Zhang, B. Shan, J. Tang, H. Liu, Z. Chen, S. Lin, W. Li and Y. Pei, *Sci. Adv.*, 2021, **7**, eabf2738.

98 A. Kumar, P. A. Vermeulen, B. J. Kooi, J. Rao, S. Schwarzmüller, O. Oeckler and G. R. Blake, *RSC Adv.*, 2018, **8**, 42322–42328.

99 E. M. Levin, S. L. Bud'ko and K. Schmidt-Rohr, *Adv. Funct. Mater.*, 2012, **22**, 2766–2774.

100 E. M. Levin, B. A. Cook, J. L. Harringa, S. L. Bud'ko, R. Venkatasubramanian and K. Schmidt-Rohr, *Adv. Funct. Mater.*, 2011, **21**, 441–447.

101 H.-X. Liu, X.-Y. Zhang, Z.-L. Bu, W. Li and Y.-Z. Pei, *Rare Met.*, 2022, **41**, 921–930.

102 X. Shi, J. R. Salvador, J. Yang and H. Wang, *Sci. Adv. Mater.*, 2011, **3**, 667–671.

103 T. Schröder, S. Schwarzmüller, C. Stiewe, J. de Boor, M. Hölzel and O. Oeckler, *Inorg. Chem.*, 2013, **52**, 11288–11294.

104 T. Schröder, T. Rosenthal, N. Giesbrecht, S. Maier, E.-W. Scheidt, W. Scherer, G. J. Snyder, W. Schnick and O. Oeckler, *J. Mater. Chem. A*, 2014, **2**, 6384–6395.

105 C. Rodenkirchen, M. Cagnoni, S. Jakobs, Y. Cheng, J. Keutgen, Y. Yu, M. Wuttig and O. Cojocaru-Mirédin, *Adv. Funct. Mater.*, 2020, **30**, 1910039.

106 T. Zhu, H. Gao, Y. Chen and X. Zhao, *J. Mater. Chem. A*, 2014, **2**, 3251–3256.

107 G. J. Snyder and T. S. Ursell, *Phys. Rev. Lett.*, 2003, **91**, 148301.

108 A. M. Abd El-Hameed, *NRIAG J. Astron. Geophys.*, 2022, **11**, 313–324.

109 B. Cai, H. Hu, H.-L. Zhuang and J.-F. Li, *J. Alloys Compd.*, 2019, **806**, 471–486.

110 C. Gayner and K. K. Kar, *Prog. Mater. Sci.*, 2016, **83**, 330–382.

111 B. Poudel, Q. Hao, Y. Ma, Y. Lan, A. Minnich, B. Yu, X. Yan, D. Wang, A. Muto, D. Vashaee, X. Chen, J. Liu, M. S. Dresselhaus, G. Chen and Z. Ren, *Science*, 2008, **320**, 634–638.

112 W. Xie, J. He, H. J. Kang, X. Tang, S. Zhu, M. Laver, S. Wang, J. R. D. Copley, C. M. Brown, Q. Zhang and T. M. Tritt, *Nano Lett.*, 2010, **10**, 3283–3289.

113 B. Xu, T. Feng, M. T. Agne, L. Zhou, X. Ruan, G. J. Snyder and Y. Wu, *Angew. Chem., Int. Ed.*, 2017, **56**, 3546–3551.

114 S. I. Kim, K. H. Lee, H. A. Mun, H. S. Kim, S. W. Hwang, J. W. Roh, D. J. Yang, W. H. Shin, X. S. Li, Y. H. Lee, G. J. Snyder and S. W. Kim, *Science*, 2015, **348**, 109–114.

115 J. Li, Q. Tan, J.-F. Li, D.-W. Liu, F. Li, Z.-Y. Li, M. Zou and K. Wang, *Adv. Funct. Mater.*, 2013, **23**, 4317–4323.

116 D.-W. Liu, J.-F. Li, C. Chen and B.-P. Zhang, *J. Electron. Mater.*, 2011, **40**, 992–998.

117 J. An, M.-K. Han and S.-J. Kim, *J. Solid State Chem.*, 2019, **270**, 407–412.
118 F. Wu, H. Song, J. Jia and X. Hu, *Prog. Nat. Sci.: Mater. Int.*, 2013, **23**, 408–412.
119 N. K. Singh, J. Pandey, S. Acharya and A. Soni, *J. Alloys Compd.*, 2018, **746**, 350–355.
120 Y. Saberi and S. A. Sajjadi, *J. Alloys Compd.*, 2022, **904**, 163918.
121 J. Mao, G. Chen and Z. Ren, *Nat. Mater.*, 2021, **20**, 454–461.
122 H. Wang and K. J. Leonard, *Appl. Phys. Lett.*, 2017, **111**, 043901.
123 T. Caillat, A. Borshchevsky and J. P. Fleurial, *J. Appl. Phys.*, 1996, **80**, 4442–4449.
124 W.-S. Liu, B.-P. Zhang, J.-F. Li, H.-L. Zhang and L.-D. Zhao, *J. Appl. Phys.*, 2007, **102**, 103717.
125 H. Kitagawa, M. Wakatsuki, H. Nagaoka, H. Noguchi, Y. Isoda, K. Hasezaki and Y. Noda, *J. Phys. Chem. Solids*, 2005, **66**, 1635–1639.
126 C. Stiewe, L. Bertini, M. Toprak, M. Christensen, D. Platzek, S. Williams, C. Gatti, E. Müller, B. B. Iversen, M. Muhammed and M. Rowe, *J. Appl. Phys.*, 2005, **97**, 044317.
127 X. Su, H. Li, Y. Yan, G. Wang, H. Chi, X. Zhou, X. Tang, Q. Zhang and C. Uher, *Acta Mater.*, 2012, **60**, 3536–3544.
128 J. Zhang, B. Xu, L.-M. Wang, D. Yu, J. Yang, F. Yu, Z. Liu, J. He, B. Wen and Y. Tian, *Acta Mater.*, 2012, **60**, 1246–1251.
129 B. C. Sales, D. Mandrus and R. K. Williams, *Science*, 1996, **272**, 1325–1328.
130 V. Trivedi, M. Battabyal, P. Balasubramanian, G. M. Muralikrishna, P. K. Jain and R. Gopalan, *Sustainable Energy Fuels*, 2018, **2**, 2687–2697.
131 X. Shi, J. Yang, J. R. Salvador, M. Chi, J. Y. Cho, H. Wang, S. Bai, J. Yang, W. Zhang and L. Chen, *J. Am. Chem. Soc.*, 2011, **133**, 7837–7846.
132 G. Rogl, A. Grytsiv, P. Rogl, N. Peranio, E. Bauer, M. Zehetbauer and O. Eibl, *Acta Mater.*, 2014, **63**, 30–43.
133 H. Li, X. Su, X. Tang, Q. Zhang, C. Uher, G. J. Snyder and U. Aydemir, *J. Materiomics*, 2017, **3**, 273–279.
134 R. He, G. Schierning and K. Nielsch, *Adv. Mater. Technol.*, 2018, **3**, 1700256.
135 R. Freer and A. V. Powell, *J. Mater. Chem. C*, 2020, **8**, 441–463.
136 S. Bai, L. Chen, M. Gu, J. Liao, R. Liu, J. Wu and X. Xia, *J. Mater. Res.*, 2019, **34**, 1179–1187.
137 S. Shittu, G. Li, X. Zhao and X. Ma, *Appl. Energy*, 2020, **268**, 115075.
138 V. Parsonnet, J. Driller, D. Cook and S. A. Rizvi, *Pacing and Clinical Electrophysiology*, 2006, **29**(2), 195–200.
139 Z. Wu, S. Zhang, Z. Liu, E. Mu and Z. Hu, *Nano Energy*, 2022, **91**, 106692.
140 Z. Yuan, K. Liu, Z. Xu, H. Wang, Y. Liu and X. Tang, *Adv. Astronaut. Sci. Technol.*, 2020, **3**, 157–163.
141 K. Liu, X. Tang, Y. Liu, Z. Xu, Z. Yuan, D. Ji and S. Ramakrishna, *Appl. Energy*, 2020, **280**, 115907.